

Secret Key Rate Limits in Coexisting Classical–Quantum Optical Links

Lucas Alves Zischler, *Student Member, IEEE*, Amirhossein Ghazisaeidi, *Senior Member, IEEE, Fellow, Optica*, Antonio Mecozzi, *Fellow, IEEE, Optica*, and Cristian Antonelli, *Senior Member, IEEE, Fellow, Optica*

Abstract—Classical-quantum coexistence enables cost-effective transmission of data and quantum signals over the same fiber-optic channel. Nevertheless, weak quantum-key distribution (QKD) signals are susceptible to non-linear interference generated from the classical traffic, primarily spontaneous Raman scattering (SpRS) and four-wave-mixing (FWM), as well as to unfiltered noise. In QKD protocols, increased channel loss and excess noise both reduce the secret key rates (SKRs), as illustrated in this work for the two-state BB84 and Gaussian-modulated coherent-states (GMCS) protocols. In this study, we derive closed-form expressions for evaluating the accumulated interference power from coexisting classical signals in a quantum frequency channel. Our model enables effective design of classical-quantum systems in single-mode fibers (SMFs), capturing the evolution of interference arising from the relevant physical phenomena. We utilize the model to examine frequency allocation in multiband transmission systems, demonstrating that, contrary to common practice of allocating QKD channels in the O-band, increased SKR is achieved by placing quantum channels in the upper E-/lower S-band across the relevant scenarios.

Index Terms—Non-linear interference, propagation model, co-existence, quantum communication, quantum-key distribution (QKD).

I. INTRODUCTION

QUANTUM-KEY distribution (QKD) enables secure key exchange, guaranteed by information limits at the quantum level [1]. With the rising prospect of quantum computers capable of compromising widely deployed asymmetric cryptographic schemes, QKD has attracted growing interest from both academia and industry as a means to safeguard deployed networks [2]–[5].

Among current research efforts, the majority of experimental deployments transmit quantum signals over optical fiber links. Given the similar nature between classical optical communications and QKD, it is logical to consider the coexistence of both applications within the same fiber network. Such coexistence eliminates the need for dedicated fibers and reduces deployment costs, and its feasibility has been extensively explored [6]–[12]. Nevertheless, the classical channels can severely impair the weak quantum signals.

Manuscript received XXX xx, XXXX; revised XXXXX xx, XXXX; accepted XXXX XX, XXXX. Funded by the European Union (Grant Agreement 101120422). Views and opinions expressed are, however, those of the author(s) only and do not necessarily reflect those of the European Union or REA. Neither the European Union nor the granting authority can be held responsible for them. (Corresponding Author: Lucas Alves Zischler)

Lucas Alves Zischler, Antonio Mecozzi, and Cristian Antonelli are with the Department of Physical and Chemical Sciences, University of L'Aquila, 67100 L'Aquila, Italy: (e-mail: lucas.zischler@univaq.it).

Amirhossein Ghazisaeidi is with the Nokia Bell Labs, 91300 Massy, France.

In wavelength-division multiplexed (WDM) coexistence schemes, the dominant impairments arise from linear effects, such as unfiltered amplified spontaneous emission (ASE), and from non-linear phenomena, primarily spontaneous Raman scattering (SpRS) and four-wave-mixing (FWM) [7], [13]. While linear noise can, in principle, be mitigated through sufficient filtering, non-linear effects are unavoidable in silica-core fibers. Although emerging hollow-core fiber technologies offer opportunities for coexistence with negligible non-linear interference [14], conventional single-mode fibers (SMFs) currently remain the most cost-effective and widely available solution.

The performance of a quantum channel is quantified by its secret key rate (SKR), which depends not only on the quantum transmitter and receiver parameters, but also on fiber attenuation and the noise generated from the classical channels. Several prior works have investigated the impact of classical channel parameters on quantum performance. In particular, [7] presents analytical models for SpRS and FWM interference, showing strong agreement with a coexistence experiment involving two classical channels and a BB84-encoded quantum signal, and demonstrating that FWM becomes negligible with sufficient channel spacing. In [13], the authors analyze SpRS-induced impairments and validate their model through experimental measurements of the SpRS efficiency. In [15], the authors explicitly focus on FWM impairments, combining analytical modeling with experimental measurements.

In this work, we provide closed-form analytical expressions to estimate the interference noise arising from all major sources induced by classical transmission, providing a comprehensive framework to aid practical implementation. The model accounts for unfiltered linear leakage at the classical transmitter, including both co-propagating contributions and counter-propagating noise generated by Rayleigh backscattering, as well as non-linear impairments due to SpRS and FWM. This study builds on our previous work [16], where we derived a comprehensive semi-analytical model for estimating coexistence-induced interference that has been experimentally validated in [17]. The developed model is employed to analytically evaluate the behavior of each impairment effects across different operating conditions. It is subsequently applied to quantify the impact of the fiber parameters and coexistence-induced noise on the asymptotic SKR of representative QKD protocols, namely the two-state BB84 and Gaussian-modulated coherent-states (GMCS) schemes, as examples of discrete-variable QKD (DV-QKD) and continuous-variable QKD (CV-QKD), respectively. With the derived model, we investigate

how the SKR can be optimized when the quantum channel wavelength is a free design parameter. In multi-band coexistence transmission, quantum-key distribution (QKD) channels are commonly assigned to the O-band, while classical traffic is allocated in the C-band [6], [11], [18], since this spectral separation provides sufficient spacing to mitigate non-linear impairments and equipment is readily available for these regions. Nevertheless, we find that SKRs can be improved by allocating the quantum channel to the upper E-band or lower S-band, where the attenuation penalty is reduced. As SKRs are much smaller than the transmitted classical traffic, the transmission of multiple concurrent QKD signals may be desirable in order to avoid key exhaustion. The similarity of CV-QKD systems to classical transmission devices naturally enables WDM of quantum signals, as demonstrated in [19]. Therefore, we also investigate the optimal continuous window for QKD, reaching similar agreement to the single-channel scenario. Furthermore, in multi-band classical transmission, assigning the additional classical channels to the L-band yields reduced noise in the E- and S-bands, without compromising classical transmission capacity.

II. ANALYTICAL MODEL AND EVALUATION OF COEXISTENCE IMPAIRMENTS

The quantum signal exhibits negligible non-linear interaction with the classical channels due to its low optical power. Consequently, only non-linear phenomena generated exclusively by classical signals are relevant. In addition, the transmission of quantum signals does not allow optical amplification.¹ As a result, only single-span systems are considered. Furthermore, since the quantum transmitter may be located at either end of the fiber, counter-propagating scattering effects must also be accounted.

In our previous work, we introduced a comprehensive semi-analytical model encompassing the most relevant coexistence impairments, including spatial crosstalk in novel fiber types for space-division multiplexing (SDM) transmission. The general expressions for the co-propagating and counter-propagating interference are given in [16, Eq. (10)] and [16, Eq. (33)], respectively. By restricting the analysis to the single-mode fiber scenario and neglecting double-backscattering, the non-linear interference noise experienced by a channel allocated at frequency f_i evolves as

$$\pm \frac{dP_i^{\text{Nli}}}{dz} = \begin{cases} \underbrace{-\alpha_i P_i^{\text{Nli}}}_{\text{Loss}} + \underbrace{\sum_h \eta_{ih} P_h e^{-\alpha_h z}}_{\text{SpRS}} + \underbrace{\tilde{\gamma}_i^2 \sum_{\substack{h,k,l \neq i \\ k=h+l-i}} P_h P_k P_l \rho_{ihkl}}_{\text{FWM}}, & \text{Fwd,} \\ -\alpha_i P_i^{\text{Nli}} + \sum_h \eta_{ih} P_h e^{-\alpha_h z}, & \text{Bwd,} \end{cases} \quad (1)$$

where the left-hand sign and the labels ‘‘Fwd’’ and ‘‘Bwd’’ refer, respectively, to the co- and counter-propagating noise with respect to the classical signal direction. The z -dependence of

the variables is omitted for conciseness. For the frequency f_i , the coefficient α_i denotes the frequency-dependent attenuation, and $\tilde{\gamma}_i = \frac{8}{9}\gamma_i$ is the effective non-linear coefficient, where γ_i is the single-polarization non-linear efficiency and the factor $\frac{8}{9}$ is the Manakov factor [21]. The coefficient η_{ih} is the SpRS efficiency from f_h to f_i , P_h denotes the classical signal launch power at f_h , and $\rho_{ihkl}(z)$ is the FWM efficiency given by

$$\rho_{ihkl} = \begin{cases} \zeta_h \Re \left\{ \frac{1 - e^{-\left(\frac{1}{2}\Delta\alpha_{ihkh} + j\Delta\beta_{ihkh}\right)z}}{\Delta\alpha_{ihkh} + j2\Delta\beta_{ihkh}} \right\} e^{(\Delta\alpha_{ihkh} - \alpha_i)z}, & h=l, \\ 4\Re \left\{ \frac{1 - e^{-\left(\frac{1}{2}\Delta\alpha_{ihkl} + j\Delta\beta_{ihkl}\right)z}}{\Delta\alpha_{ihkl} + j2\Delta\beta_{ihkl}} \right\} e^{(\Delta\alpha_{ihkl} - \alpha_i)z}, & h \neq l, \end{cases} \quad (2)$$

where $\Re\{\cdot\}$ is the real part, ζ_h is the kurtosis of the signal allocated at f_h [22, Table I], and $\Delta\alpha_{ihkl}$ and $\Delta\beta_{ihkl}$ are given by

$$\begin{aligned} \Delta\alpha_{ihkl} &= \alpha_i - \alpha_h - \alpha_k - \alpha_l, \\ \Delta\beta_{ihkl} &= \beta_i - \beta_h + \beta_k - \beta_l. \end{aligned} \quad (3)$$

The coefficient $\Delta\beta_{ihkl}^{(n)}$ can be approximated by its Taylor series

$$\Delta\beta_{ihkl} \approx 2\pi^2 \beta_{2,i} (f_i^2 - f_h^2 + f_k^2 - f_l^2), \quad (4)$$

where $\beta_{2,i}$ is the frequency-dependent group-velocity-dispersion parameter. For evenly spaced channels, Eq. (4) can be further simplified to

$$\Delta\beta_{ihkl} \approx 2\pi^2 \beta_{2,i} (i^2 - h^2 + k^2 - l^2) \Delta f_{\text{ch}}^2, \quad (5)$$

where Δf_{ch} is the channel spacing.

In addition to non-linear interference, without sufficient filtering, a non-negligible amount of linear leakage with optical power P_i at the quantum frequency f_i can be expected. In a counter-propagation scenario, the leaked interference can backpropagate toward the quantum receiver via Rayleigh backscattering.²

Noting that the interference powers are sufficiently weak, such that their fields do not interact non-linearly, closed-form solutions to Eq. (1) can be obtained for both propagation directions. Accounting also for a small linear leakage from the classical transmitter into the quantum channel, a closed-form expression for the total noise variance at f_i produced by the classical transmission is given by

$$P_i^{\text{Int}} = \begin{cases} \sum_{h \neq i} \eta_{ih} P_h \Omega_{ih} + \tilde{\gamma}_i^2 \sum_{\substack{h,k,l \neq i \\ k=h+l-i}} P_h P_k P_l \chi_{ihkl} + P_i e^{-\alpha_i L}, & \text{Fwd,} \\ \sum_{h \neq i} \eta_{ih} P_h \Omega_{ih} + \Gamma_i P_i \frac{1 - e^{-2\alpha_i L}}{2\alpha_i}, & \text{Bwd,} \end{cases} \quad (6)$$

where L is the link length, Γ_i is the frequency-dependent Rayleigh backscattering efficiency, Ω_{ih} accounts for the longitudinal evolution of the SpRS contribution

$$\Omega_{ih} = \begin{cases} \frac{e^{(\alpha_i - \alpha_h)L} - 1}{\alpha_i - \alpha_h} e^{-\alpha_i L}, & \text{Fwd,} \\ \frac{1 - e^{-(\alpha_i + \alpha_h)L}}{\alpha_i + \alpha_h}, & \text{Bwd,} \end{cases} \quad (7)$$

¹The discussion in this work focuses on key exchange between two peers in a single-span scenario. Some approaches extend the reach of QKD by employing trusted nodes to establish intermediate keys [3], and more sophisticated entanglement-based protocols consider an intermediate node in the quantum-key exchange [20].

²Backscattered FWM via Rayleigh scattering is possible. However, FWM is typically only relevant within the classical transmission band, where backscattered SpRS is significant, as shown further in this work. By contrast, linear leakage from the classical transmitter can occur at any frequency, therefore, it is included here.

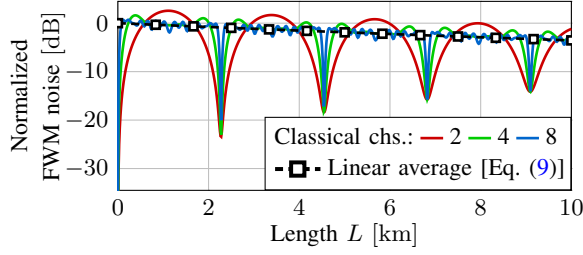


Fig. 1: Normalized FWM noise versus fiber length for the given numbers of classical channels (color-coded), together with the linearly averaged value, shown with square markers.

and χ_{ihkl} is the corresponding term for FWM, given by

$$\chi_{ihkl} = \begin{cases} \zeta_h \frac{e^{\Delta\alpha_{ihkh}L} - 2e^{\frac{1}{2}\Delta\alpha_{ihkh}L} \cos(\Delta\beta_{ihkh}L) + 1}{\Delta\alpha_{ihkh}^2 + 4\Delta\beta_{ihkh}^2} e^{-\alpha_i L}, & h = l, \\ 4 \frac{e^{\Delta\alpha_{ihkl}L} - 2e^{\frac{1}{2}\Delta\alpha_{ihkl}L} \cos(\Delta\beta_{ihkl}L) + 1}{\Delta\alpha_{ihkl}^2 + 4\Delta\beta_{ihkl}^2} e^{-\alpha_i L}, & h \neq l. \end{cases} \quad (8)$$

As shown in [23, Fig. 7] and [16, Fig. 3], the FWM component exhibits rapid longitudinal oscillations. As the oscillation period is proportional to $\Delta\beta_{ihkl}$, the interaction among many frequency terms produces an averaging effect. By linearly averaging the FWM coefficients, a simplified approximation can be obtained, given by

$$\chi_{ihkl} \approx \tilde{\chi}_{ihkl} = \begin{cases} \zeta_h \frac{e^{\Delta\alpha_{ihkh}L} + 1}{\Delta\alpha_{ihkh}^2 + 4\Delta\beta_{ihkh}^2} e^{-\alpha_i L}, & h = l, \\ 4 \frac{e^{\Delta\alpha_{ihkl}L} + 1}{\Delta\alpha_{ihkl}^2 + 4\Delta\beta_{ihkl}^2} e^{-\alpha_i L}, & h \neq l. \end{cases} \quad (9)$$

Figure 1 shows the relative FWM longitudinal intensity for an increasing count of classical channels, normalized to their respective linear averages. The classical channels are allocated at the upper frequency slots above the quantum channel. The plots assume a fixed attenuation of $\alpha = 0.2$ dB/km, a channel spacing of $\Delta f_{ch} = 50$ GHz, and a group-velocity-dispersion parameter of $\beta_2 = -28$ ps²/km. As the channel count increases, with as few as 8 channels, the FWM evolution is closely represented by the approximation.

A. Dependence on fiber length

In the counter-propagating scenario, the effects accumulate up to a saturation level, whereas in the co-propagating case all contributions are attenuated by fiber loss for sufficiently long lengths.

Both FWM and co-propagating linear leakage generally decay with length, whereas the co-propagating SpRS contribution initially grows and peaks at distance L_{Pk} . The peak length L_{Pk} is obtained from the co-propagating SpRS term in Eq. (6) for the interference contribution from f_h to f_i as

$$\left. \frac{d}{dL} \eta_{ih} P_h \frac{e^{(\alpha_i - \alpha_h)L} - 1}{\alpha_i - \alpha_h} e^{-\alpha_i L} \right|_{L=L_{Pk}} = 0, \quad (10)$$

after which, through algebraic manipulation, the expression for L_{Pk} is obtained as

$$L_{Pk} = \frac{1}{\alpha_h - \alpha_i} \ln \left(\frac{\alpha_h}{\alpha_i} \right), \quad \lim_{\alpha_h \rightarrow \alpha_i} L_{Pk} = \frac{1}{\alpha_i}. \quad (11)$$

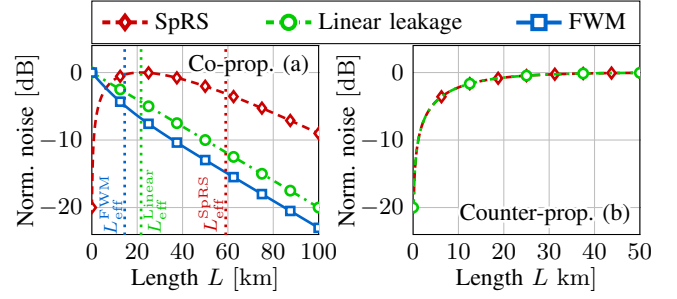


Fig. 2: Normalized interference versus fiber length for the different sources (distinguished by markers) in (a) co-propagating and (b) counter-propagating scenarios.

The co-propagating interference contributions evolve at distinct rates along the fiber, and an effective length can be defined for each contribution. The effective length is computed by integrating the corresponding contribution over the fiber length and normalizing it to its peak value. For the effects considered here, for each frequency contribution, the effective length at the quantum channel is given by

$$\begin{aligned} L_{\text{eff}}^{\text{SpRS}} &= \frac{\alpha_i(1 - e^{-\alpha_n L}) - \alpha_h(1 - e^{-\alpha_i L})}{\alpha_i \alpha_h (e^{-\alpha_n L_{Pk}} - e^{-\alpha_i L_{Pk}})}, \\ L_{\text{eff}}^{\text{FWM}} &= \frac{1}{2} \left[\frac{e^{(\Delta\alpha_{ihkl} - \alpha_i)L} - 1}{\Delta\alpha_{ihkl} - \alpha_i} + \frac{1 - e^{-\alpha_i L}}{\alpha_i} \right], \\ L_{\text{eff}}^{\text{Linear}} &= \frac{1 - e^{-\alpha_i L}}{\alpha_i}, \end{aligned} \quad (12)$$

where, for the FWM term, the approximation in Eq. (9) is used.

The counter-propagating SpRS noise and the Rayleigh-backscattered linear noise grow with fiber length at similar rates, scaling as $(1 - e^{-(\alpha_i + \alpha_h)L})$ and $(1 - e^{-2\alpha_i L})$, respectively.

The normalized longitudinal dependence of all contributions depends only on attenuation. Figure 2 shows how each interference contribution evolves with fiber length, normalized to its peak value. Fiber attenuation is assumed constant and equal to $\alpha = 0.2$ dB/km for this purpose. In Fig. 2(a) we plot the evolution of the co-propagating interference. The FWM contribution is strongly concentrated at short distances, whereas SpRS is dominant at long reaches, with the linear leakage contribution in between. Dotted lines indicate the asymptotic effective lengths ($L \rightarrow \infty$) of the co-propagating contributions. Both counter-propagating contributions, shown in Fig. 2(b), evolve at similar rates for the parameters considered, converging to a saturation level after ~ 20 km.

B. Wavelength dependence

Many works have investigated multi-band transmission for coexistence schemes [6], [11], [12], [18], as non-linear interference can be significantly mitigated by increasing the spacing between classical and quantum channels. Nevertheless, fiber parameters can vary substantially between bands, requiring careful characterization.

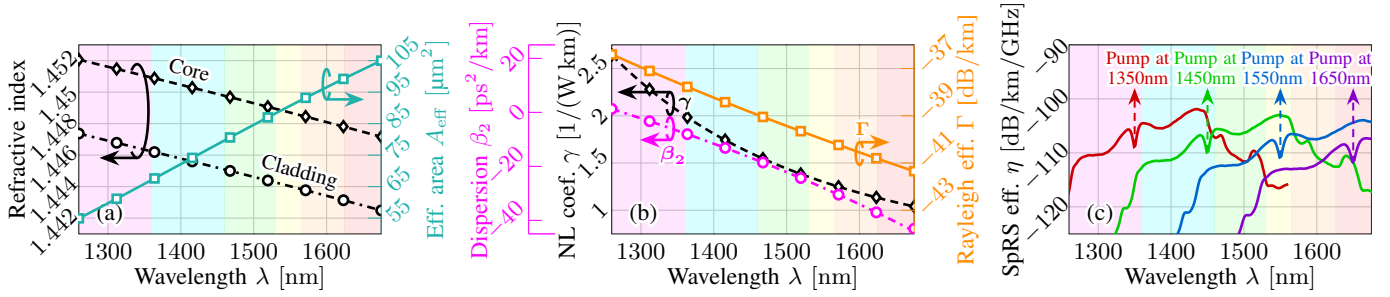


Fig. 3: (a) Refractive index and effective area of the considered fiber. (b) Wavelength dependence of the group-velocity dispersion, non-linear coefficient, and Rayleigh efficiency. (c) SpRS efficiency for different pump wavelengths (color-coded). The shaded background regions indicate the transmission bands. From left to right, the colors correspond to the O-, E-, S-, C-, L-, and U-bands.

Figure 3(a) shows the frequency-dependent refractive index profile and effective area A_{eff} for a 10 μm -core step-index fiber with a germanium-doped core and a core-to-cladding index ratio of 0.31%. The refractive index is calculated from Sellmeier's formula, with coefficients given in [24, Table 8].

In Fig. 3(b), we plot the fiber's material group-velocity dispersion (β_2), non-linear coefficient (γ), and Rayleigh scattering efficiency (Γ). The non-linear coefficient and Rayleigh efficiency depend on the material properties as well as the refractive profile, and are considered to be $1.3 \text{ W}^{-1} \text{ km}^{-1}$ and $-40 \text{ dB}/\text{km}$ at 1550 nm, respectively, scaling with wavelength as $\gamma \propto (\lambda A_{\text{eff}})^{-1}$ and $\Gamma \propto \lambda^{-4}$ [25].

The dispersion is calculated from the derivatives of the mode propagation constant, typically crossing the axis within the O-band and increasing in magnitude with wavelength. As the dispersion coefficient increases, FWM is reduced, as is known and evident in Eqs. (8) and (5). Similarly, the non-linearity coefficient decreases as the wavelength and effective area increase, and the Rayleigh scattering efficiency decays rapidly with wavelength.

Figure 3(c) shows the SpRS efficiency for different pump channel wavelengths. With the exception of narrow peaks that matter in single-channel scenarios [18], SpRS interference is overall a broadband effect. The curves plotted in Fig. 3(c) are derived from the Raman gain efficiency provided in [26], [27], using the analytical expression in [16, Eq. (8)] to obtain the SpRS efficiency, assuming the waveguide is at 300 K. The SpRS efficiency scales as $\eta_{ih} \propto (\lambda_i A_{\text{eff},i,h})^{-1}$, where $A_{\text{eff},i,h}$ is the effective cross-mode area between the lateral field profiles at f_i and f_h [28, Eq. (7)], which varies non-negligibly across different bands.

The SpRS efficiency decreases at anti-Stokes frequencies and as the pump wavelength increases. Therefore, allocating the stronger signals at longer wavelengths reduces interference in channels at shorter wavelengths, compared with the opposite configuration.

As observed in Fig. 3, interference effects generally decrease as the wavelengths of the interference-inducing channels increase. Nevertheless, as discussed further, fiber attenuation also increases beyond its minimum in the C- and L-bands, indicating a non-trivial optimal frequency placement.

C. Dependence on classical signals

The interference effects exhibit different dependencies on the classical signal parameters. For the FWM contribution, the propagation-constant mismatch $\Delta\beta_{ihkl}$ defines both the period of the longitudinal oscillations and the resulting interference intensity. For a fixed WDM grid, and using the approximation given in (5) within Eq. (9), the interference intensity is found to be proportional to both the channel-index mismatch and the channel spacing. Figure 4(a) illustrates the reduction of FWM interference as a function of channel spacing, for different values of channel-index mismatch. The curves assume $\alpha = 0.2 \text{ dB}/\text{km}$ and $\beta_2 = -28 \text{ ps}^2/\text{km}$, and are normalized to their asymptotic peak values at $\Delta f_{\text{ch}} \rightarrow 0 \text{ GHz}$. As the channel spacing increases, the FWM contribution decreases sharply, with a similar reduction observed for increasing channel-index mismatch. Consequently, increasing the separation between the quantum and classical channels by a few gigahertz can significantly suppress FWM. This result was presented in a similar form in [7, Fig. 1].

As only channel combinations satisfying the phase-matching condition $i - h + k - l = 0$ contribute to FWM, the overall interference intensity depends on the placement of the quantum channel in the WDM grid. Considering N evenly

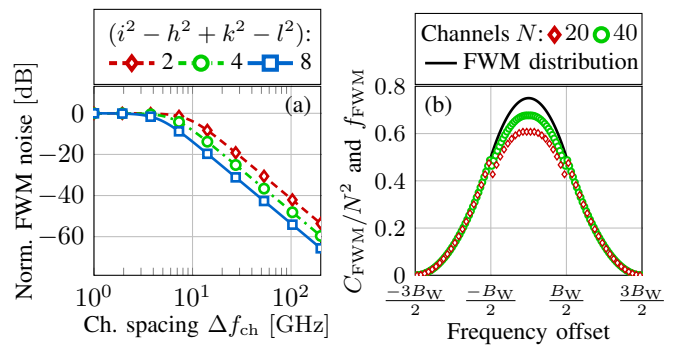


Fig. 4: (a) Normalized FWM interference as a function of channel spacing for different index-mismatch values ($i^2 - h^2 + k^2 - l^2$). (b) Normalized FWM matching count C_{FWM} from (13) and the corresponding continuous distribution f_{FWM} from (14).

spaced frequency channels within a total bandwidth B_W , the number of FWM interference components affecting a channel with index i is given by (derivation in Appendix A)

$$C_{\text{FWM}} = \begin{cases} \frac{N^2 + N + 2Ni + i^2}{2}, & i < 0, \\ \frac{N^2 - 5N + 2Ni - 2i - 2i^2 + 4 + 2|2i - N + 1|}{2}, & 0 \leq i < N, \\ \frac{4N^2 - 2N - 4Ni + i^2}{2}, & N \leq i. \end{cases} \quad (13)$$

As $N \rightarrow \infty$, Eq. (13) admits a continuous form, representing the combination count as a probability distribution normalized to the total bandwidth B_W , given by

$$f_{\text{FWM}} = \begin{cases} \frac{1}{2} \left(\Delta_i + \frac{3}{2}\right)^2, & \Delta_i < -\frac{1}{2}, \\ -\Delta_i^2 + \frac{3}{4}, & -\frac{1}{2} < \Delta_i < \frac{1}{2}, \\ \frac{1}{2} \left(\Delta_i - \frac{3}{2}\right)^2, & \Delta_i > \frac{1}{2}, \end{cases} \quad (14)$$

where $\Delta_i = \frac{f_i - f_c}{B_W}$, with f_c denoting the center frequency of the transmission band. The distribution is non-zero only within the interval $\Delta_i \in \left(-\frac{3}{2}, \frac{3}{2}\right)$.

In Fig. 4(b), we plot the normalized FWM density for different channel counts N , and the asymptotic probability distribution. For finite channel counts, the FWM intensity within the classical transmission band is reduced, since one classical signal must be removed to allocate the quantum channel. The distribution peaks at the center of the transmission band and decays by $\sim 33\%$ at the band edges, eventually decaying to zero at a separation of B_W from the classical signals.

The interference effects also exhibit distinct dependencies on channel power. While SpRS and linear noise scale linearly, FWM scales with the third power of the channel power, as can be directly inferred from Eq. (6).

In the counter-propagating configuration, Rayleigh-backscattered linear noise and SpRS grow at similar rates with channel power and length. The dominant effect is determined by the ratio of the SpRS and Rayleigh efficiencies, as well as by the relative channel powers and the level of linear leakage. The linear leakage can be reduced by increasing the filter order and is often partially suppressed by the multiplexer, but it cannot be completely nullified.

III. QUANTUM CHANNEL IMPAIRMENTS

Noisy photons impair the QKD signal on different scales, depending on the protocol. In DV-QKD, information is encoded in the individual photons, resulting in a relatively low tolerance to noise. In contrast, CV-QKD protocols encode information in weak coherent states, which are transmitted at higher power levels than DV-QKD signals and therefore tolerates higher levels of interference. In this section, we evaluate the asymptotic SKR limits under a noisy and lossy channel using BB84 and GMCS as representative examples of DV- and CV-QKD protocols, respectively.

We assume ideal QKD transmitters and receivers, such that the resulting asymptotic limits are determined solely by the fiber-channel impairments. The noise is assumed to be randomly polarized, Gaussian distributed, and spectrally flat within the quantum channel bandwidth. Under these assump-

tions, the noise power spectral density (PSD) at frequency f_i is given by

$$S_i^{\text{Int}} = \frac{P_i^{\text{Int}}}{B_{\text{ch}}}, \quad (15)$$

where B_{ch} denotes the bandwidth of the WDM grid slots.

In this work, the SKR is defined as the secure key fraction (measured in bits per symbol), following conventional entropy-based definitions of theoretical QKD works [29], [30]. Assuming an ideal error-correction algorithm, the asymptotic rate of secret bits for a given scheme is then obtained by multiplying the SKR by the symbol rate.

A. In DV-QKD protocols

In the original BB84 protocol, the transmitter sends a sequence of photons randomly alternating between two mutually unbiased bases, with information encoded in the photon state [31]. At the receiver, photons are measured in randomly selected bases. Coincidence events from mismatched bases are discarded during post-processing.

Assuming an ideal, lossless, and noiseless QKD transmitter and receiver, the resulting quantum bit error rate (QBER) is given by (detailed in Appendix B)

$$\text{QBER} = \frac{S_i^{\text{Int}} R_{\text{det}}}{hf_i T_i + S_i^{\text{Int}} R_{\text{det}}}, \quad (16)$$

where $T_i = e^{-\alpha_i L}$ is the channel transmittance, and $R_{\text{det}} = B_{\text{det}} \tau_{\text{det}}$ is the collection factor that determines the fraction of received noise power integrated into a single detection bin³. Here, B_{det} denotes the quantum receiver bandwidth, and τ_{det} is the single-photon detector measurement time window. The factor R_{det} results in a linear scaling of the noise PSD and, unless otherwise specified, we assume $R_{\text{det}} = 1$ throughout this work for simplicity.

The asymptotic SKR is related to the QBER as [29]

$$r_{\text{BB84}} = \frac{T_i}{2} [1 - 2H_2(\text{QBER})], \quad (17)$$

where $H_2(\cdot)$ is the binary Shannon entropy function, the factor $\frac{1}{2}$ accounts for the sifting step, and T_i denotes the channel transmittance, accounting for all propagation losses.

B. In CV-QKD protocols

In CV-QKD, information is encoded in continuous quantum states. Specifically, in GMCS, the bit sequence is modulated in coherent Gaussian-distributed symbols [32].

In calculations, power values are normalized to the shot-noise variance, which is proportional to the local oscillator power [33].

The excess noise comprises multiple contributions as detailed in [33], one of which is the coexistence-induced impairment. To isolate the effects of the coexisting classical signals, in this study, we disregard all other noise sources ($\xi_i = \xi_{\text{coex},i}$).

³The factor R_{det} can theoretically be zero, since amplitude-encoded signals (such as polarization-basis or time-bin BB84) can have negligible bandwidth, making it theoretically possible with perfect synchronization and no timing jitter to filter only signal photons. In practice, however, receivers integrate over a finite time window and thus unavoidably collect some coexistence-induced noise photons.

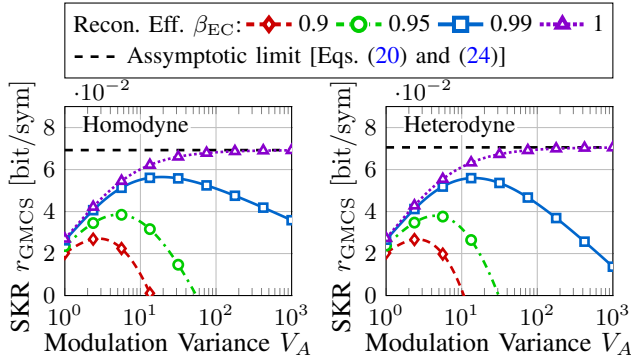


Fig. 5: Secret key rate of GMCS for homodyne- and heterodyne-detected schemes as a function of modulation variance. The transmitter and receivers are assumed as ideal, lossless, and noiseless. Channel parameters are $T = -10$ dB and $\xi = 10^{-3}$.

Under the assumptions of white, Gaussian distributed coexistence-induced noise and a flat receiver frequency response, the coexistence noise variance, expressed in shot-noise units, is given by (see Appendix C)

$$\xi_{\text{coex},i} = \frac{S_i^{\text{Int}}}{2hf_i}. \quad (18)$$

In reverse reconciliation protocols, the asymptotic rate of secret bits per transmitted pulse is given by

$$r_{\text{GMCS}} = \beta_{\text{EC}} I_{AB} - \chi_{EB}, \quad (19)$$

where $\beta_{\text{EC}} \leq 1$ is the error-correction reconciliation efficiency, I_{AB} is the mutual information between the transmitter and receiver, and χ_{EB} is the Holevo bound between an ideal eavesdropper and the receiver.

Figure 5 plots the SKR versus modulation variance V_A for both homodyne- and heterodyne-detected GMCS. With ideal reconciliation ($\beta_{\text{EC}} = 1$), the information rate and the Holevo bound increase at the same rate for large V_A , such that the SKR approaches an upper bound as $V_A \rightarrow \infty$, as shown in the figure. Practical coding schemes cannot reach this asymptotic limit, but current coding schemes have reported efficiencies up to 0.99 [34], [35]. Assuming ideal transmitters and receivers, this asymptotic limit represents a theoretical upper bound for SKRs, limited only by the lossy and noisy channel.

Assuming the signal as Nyquist-shaped with a symbol rate equal to the detector bandwidth (sinc-shaped pulses with zero roll-off), the asymptotic SKR for $\beta_{\text{EC}} = 1$ and $V_A \rightarrow \infty$ in a homodyne-detected configuration is given by (derivation in Appendix D)

$$r_{\text{GMCS}} = \frac{1}{2} \log_2 \left[\frac{T_i \phi}{(\xi_i + 1)(1 - T_i)} \right] - h_2(\omega), \quad (20)$$

with ϕ given by

$$\phi = T_i \omega + (1 - T_i)[2\omega - 1 + (\xi_i + \mu)/T_i], \quad (21)$$

where $\mu = 1$ for homodyne and $\mu = 2$ for heterodyne detection, and where ω is given by

$$\omega = \frac{\xi_i}{1 - T_i} + 1, \quad (22)$$

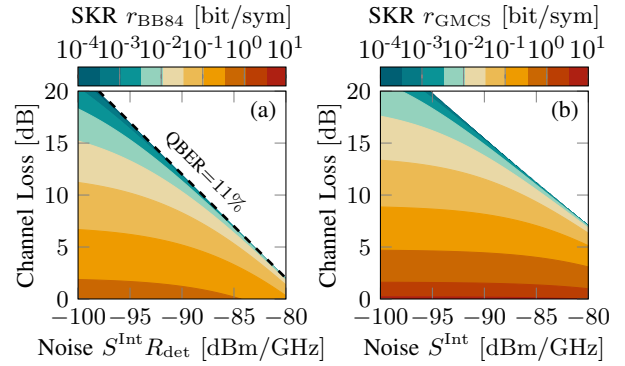


Fig. 6: Asymptotic SKRs as a function of channel loss and noise for (a) BB84 and (b) heterodyne-detected GMCS protocols.

and $h_2(\cdot)$ is given as

$$h_2(x) = \frac{x+1}{2} \log_2 \left(\frac{x+1}{2} \right) - \frac{x-1}{2} \log_2 \left(\frac{x-1}{2} \right). \quad (23)$$

For heterodyne detection, the asymptotic SKR is given by

$$r_{\text{GMCS}} = \log_2 \left[\frac{T_i}{(\xi_i + 2)(1 - T)} \right] - h_2(\omega) + h_2 \left(\frac{\xi + 2 - T}{T} \right) + 1 - \log_2(e). \quad (24)$$

IV. CHANNEL'S SKR LIMITS AND INTERFERENCE MITIGATION

Under a lossy Gaussian-noise channel, the asymptotic limits of GMCS depend solely on the channel parameters, whereas the asymptotic limits of BB84 also depend on the collection factor. Figure 6 illustrates how the asymptotic SKRs of both BB84 and GMCS vary with different levels of loss and noise. In Fig. 6(a), it is highlighted the region where QBER reaches the known threshold of 11%, above which no error-correction algorithm can recover the secret key [29]. Both BB84 and GMCS scale similarly with respect to loss and noise, noting that GMCS achieve higher rates at low loss, as it can transmit more than a single bit per pulse.

In WDM classical-quantum links, the frequency dependence of both interference and attenuation affects QKD protocols with different scaling. The frequency dependence of the interference effects was discussed in Section II. While interference decreases at longer wavelengths, the attenuation profile of silica-core fibers exhibits a minimum in the C- and L-bands, as illustrated in Fig. 7 for different water-peak levels.

In Fig. 8(a), we plot the interference noise as a function of wavelength for a representative C-band-loaded scenario. Curves show the total noise and the individual contributions from each phenomena, calculated from Eq. (6). Noise within the transmission band assumes that the corresponding classical channel is deallocated. The curves consider a fiber length of $L = 25$ km, and a channel spacing of $\Delta f_{\text{ch}} = 50$ GHz with 88 polarization-multiplexed 16-QAM-shaped classical channels in the C-band. Each classical frequency channel is launched at $P = -2$ dBm, summed over both polarizations. Assuming

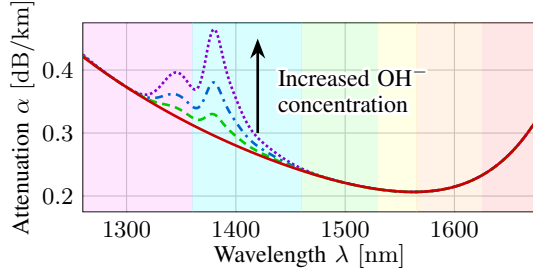


Fig. 7: Fiber attenuation profiles for varying OH^- concentrations, distinguished by line style. Curves are analytically calculated according to [36].

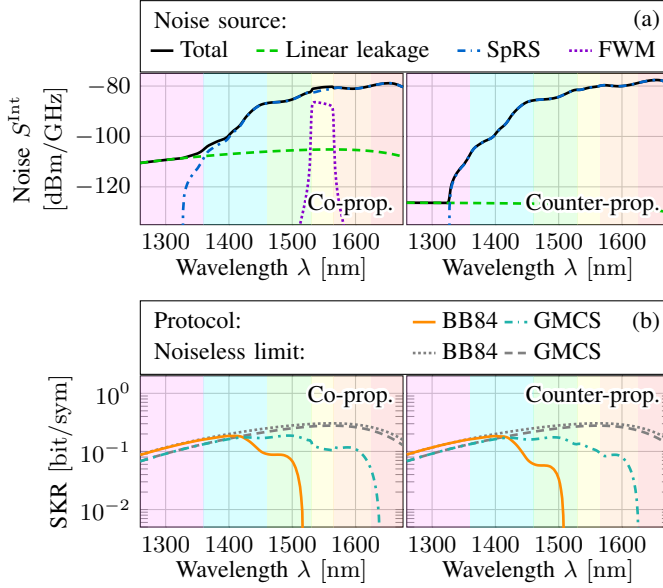


Fig. 8: (a) Noise contributions from different sources and (b) asymptotic SKRs considering the total interference in co- and counter-propagating scenarios, plotted alongside their respective loss-limited reference curves.

a 32 GBaud symbol rate with 0.1 roll-off factor, a flat-gain pre-amplifier with 7 dB noise figure, and a minimum per-channel received power of -5 dBm, with [37, Eq. (40)], the classical signals yield a combined achievable information rate (AIR) of 22.53 Tbit/s. It is assumed a linear noise floor of -100 dBm/GHz at the classical transmitter.⁴ Frequency-dependent parameters are given in Fig. 3, with attenuation corresponding to the OH^- -peak-absent case shown in Fig. 7.

The overall dominant noise source in both co- and counter-propagating scenarios is SpRS. As expected from Fig. 3(c), SpRS noise is more significant in the L- and U-bands compared to the lower bands. Linear leakage is substantially mitigated by the Rayleigh factor in a counter-propagating configuration, whereas SpRS remains at equal intensity. In the co-propagating configuration, FWM exhibits a non-negligible magnitude within the transmission band, comparable to the

⁴This assumes a ~ 30 dB filter at the quantum channel frequency, with unfiltered ASE noise floor ~ 20 dB below the transmission band PSD, as measured from a reference C-band amplifier [17].

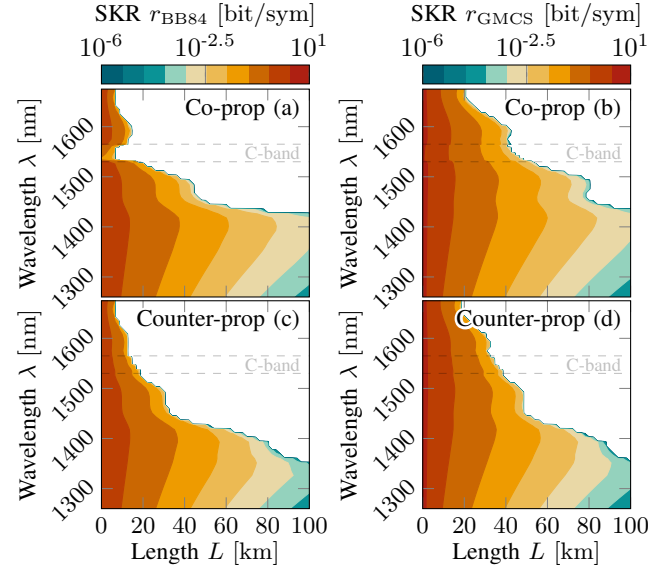


Fig. 9: Asymptotic SKRs as a function of the quantum channel wavelength and fiber length. Secret key rate curves are shown for (a, c) BB84 and (b, d) GMCS protocols, in both propagation directions.

scale of SpRS. Consistent with Fig. 4(b), FWM is concentrated within the transmission band and negligible in the adjacent bands.

Figure 8(b) shows the asymptotic SKRs of the BB84 and GMCS protocols derived from the total noise curves in Fig. 8(a). Within the O- and most of the E-band, the SKRs reach the noiseless limit, indicating that noise impairments are negligible in this region. In this loss-limited region, BB84 and GMCS rates are similar. In the S- and upper bands, GMCS rates remain high and dropping near the U-band, as the protocol can tolerate increased noise, whereas BB84 rates drop sharply in the lower S-band.

Figure 9 shows the SKRs as a function of wavelength and fiber length, for the same classical transmission configuration as in Fig. 8. Across protocols and propagation directions, the region below 1400 nm remains unchanged, as coexistence noise is minimal and SKRs are limited by the channel loss. For the given classical configuration, long distance QKD transmission is unachievable at higher wavelength.

Regardless of the protocol, Fig. 8(b) and Fig. 9 shows that SKRs peak near 1400 nm, within the E-band, for a given fiber length, due to the combination of lower noise and lower loss. As the water-peaks are located in the lower E-band, Fig. 10 illustrates how SKRs vary in this region as the OH^- concentration increases, from the attenuation curves plotted in Fig. 7 for $L = 25$ km.

The region near the OH^- peaks may be undesirable for wide-scale deployment of QKD services, as performance is highly dependent on fiber grade. Nevertheless, the upper E-band and lower S-band still provide higher SKRs compared to the typical O-band, and are mostly unaffected by OH^- concentration. These findings can be leveraged to improve SKRs in future commercial coexistence deployments by tailoring QKD

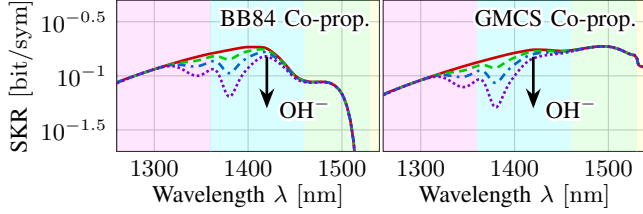


Fig. 10: Asymptotic SKRs for different OH^- concentrations, with line styles corresponding to the attenuation curves shown in Fig. 7.

devices and components for operation within the upper E-band and lower S-band.

In Fig. 11, we plot the band-averaged asymptotic GMCS SKR over a dedicated QKD band as a function of its center wavelength, for the considered bandwidths. The classical transmission parameters are as previously defined, and it is considered no overlap between the classical and QKD bands. Figure 11(a), which considers the attenuation profile without the OH^- absorption peak, we observe overlap between the curves. In contrast, Fig. 11(b) shows that the sharp water-peak-induced drops are progressively smoothed as the QKD bandwidth increases. Overall, the behaviour of the QKD band follows that of a single channel. However, the increased bandwidth averages out localized drops, yielding a more uniform aggregate SKR.

As excess noise in CV-QKD arises from multiple sources, Fig. 12 shows SKRs under additional flat excess noise, simulating further impairments. This additional noise shifts the SKRs for the given configurations, though they remain close to the limit set by coexistence-induced impairment alone.

Finally, we consider scenarios in which classical traffic is transmitted in other bands than the C-band. Figure 13 plots the noise spectral contributions for classical signals allocated in the S-, C-, or L-band and the corresponding SKRs. The system parameters are the same as those for Fig. 8, with the L-band supporting 142 channels (AIR: 36.35 Tbit/s) and the S-band 188 channels (AIR: 48.13 Tbit/s). Interference increases from

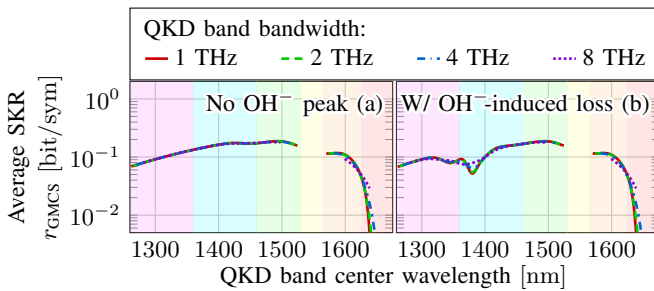


Fig. 11: Asymptotic co-propagating GMCS SKRs averaged over a QKD WDM band as a function of the band center wavelength. The curves in (a) consider the attenuation profile without the OH^- absorption peak shown in Fig. 7, while (b) considers the corresponding profile with the highest absorption peak.

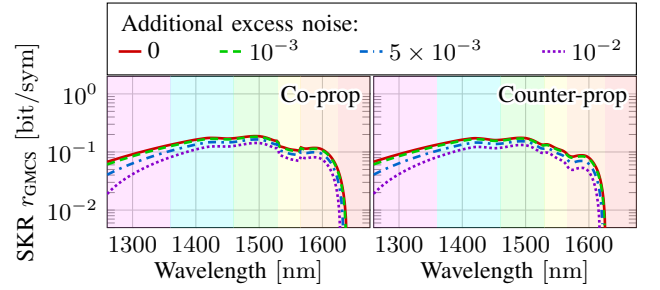


Fig. 12: Asymptotic GMCS SKRs in both propagating directions, accounting for the additional flat excess-noise values given in the legend.

the C-band to the S-band due to higher total power and non-linearities. Notably, SpRS from the S-band dominates across the entire E-band, significantly reducing SKRs. Despite the increased channel count and power, interference from the L-band remains comparable to that generated by the C-band, due to reduced non-linearities. These findings indicate that expansion or reallocation toward the L-band notably improves the combined classical-quantum throughput, whereas S-band signals impose penalties even on O-band quantum channels.

V. CONCLUSION

Weak QKD signals in classical-quantum WDM links are primarily affected by unfiltered linear leakage, SpRS, and FWM. Each of these phenomena exhibits distinct spectral and longitudinal scaling and may become significant under different scenarios. Furthermore, the frequency dependence of fiber attenuation leads to non-trivial optimal configurations for QKD channel allocation.

We analyze how the two-state BB84 and GMCS protocols scale asymptotically with noise. The presented analytical models enable quick assessment of the channel and identification of optimal configurations.

As demonstrated in representative scenarios and supported by the theory, improved SKRs can be achieved in the upper

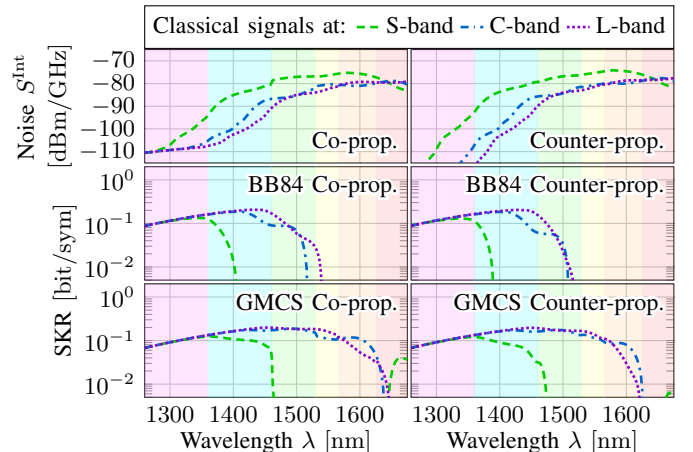


Fig. 13: Co- and counter-propagating noise and asymptotic SKRs for classical signals allocated in different transmission bands.

E-band, where interference from the C-band is sufficiently suppressed and attenuation is lower than in the typically utilized O-band. The assertion sustains even when a continuous band is dedicated for WDM quantum channels. Additionally, allocating classical traffic to the L-band further suppresses SpRS in the E- and lower S-bands. Contrary to conventional O-C quantum-classical coexistence schemes, E-L or S-L allocation can increase SKRs without detriment to classical transmission rates.

APPENDIX A DISTRIBUTION OF FWM CONTRIBUTIONS

Considering a transmission band with N evenly spaced channels. The interference channel indices are given by $h, k, l \in [0, N - 1]$, while FWM interference is limited to channels $i \in [-N + 1, 2N - 2]$. From the phase-matching condition ($i - h + k - l = 0$), the number of FWM contributions at a given index i , denoted C_i , where k is determined by the remaining indices, is given by the count of pairs (h, l) that satisfy

$$i \leq h + l < i + N. \quad (25)$$

The number of combinations of (h, l) that satisfy a given sum $x = h + l$, for $x \in (0, 2N - 2)$, is

$$C_x = \min(x + 1, 2N - x - 1), \quad (26)$$

therefore, the total number of combinations C_i that satisfy (25) is given by

$$C_i = \begin{cases} \sum_{x=0}^{N+i-1} x + 1, & i < 0, \\ \sum_{x=i}^{N+i-1} \min(x + 1, 2N - x - 1), & 0 \leq i < N, \\ \sum_{x=i}^{2*N-2} 2 * N - x - 1, & N \leq i, \end{cases} \quad (27)$$

where after simple manipulations, it can be expressed as

$$C_i = \begin{cases} \frac{N^2 + N + 2Ni + i + i^2}{2}, & i < 0, \\ \frac{N^2 + N + 2Ni - 2i - 2i^2}{2}, & 0 \leq i < N, \\ \frac{4N^2 - 2N - 4Ni + i + i^2}{2}, & N \leq i. \end{cases} \quad (28)$$

As the quantum signal is weak and therefore does not participate in the FWM interaction, contributions where $h = i$, $k = i$, and/or $l = i$ should be excluded. This only applies for $0 \leq i < N$. The number of valid combinations that satisfy this criteria is

$$C_{h=i} = C_{l=i} = N - 1, \quad C_{k=i} = 2 \min(i, N - i - 1). \quad (29)$$

After some manipulation, the number of FWM contributions in a dedicated quantum channel, excluding overlapping terms, is given by (13).

APPENDIX B ASYMPTOTIC TWO-STATE BB84 SKRS

Considering only photons on the correct encoding basis, the received photon rate is given by

$$N^{\text{RX}} = \eta_{\text{RX}} T_i N^{\text{TX}}, \quad (30)$$

where η_{RX} is the receiver efficiency and N^{TX} is the transmitted QKD photon rate.

The single-photon receiver uses a detection window of width τ_{det} , which, in the absence of timing jitter, should fully capture a single signal pulse. In time bin protocols, the measurement bases correspond to distinct time offsets within this window.

Interference photons measured within the detection window τ_{det} are Poisson-distributed. The mean number of interference photons within the window τ_{det} at frequency f_i is proportional to the received noise power as

$$\bar{N}_i^{\text{Int}} = \frac{P_i^{\text{Int}} B_{\text{det}} \tau_{\text{det}}}{B_{\text{ch}} h f_i}, \quad (31)$$

where B_{det} is the receiver's measurable bandwidth. Considering that one photon is transmitted per measurement interval (multiple-photon events should ideally be discarded [38]), and neglecting optical shot noise, the mean number of received photon signal is $\eta_{\text{RX}} T_i$, and the probability of a corrupted measurement is given by the QBER as

$$\text{QBER} = \frac{\eta_{\text{RX}} \bar{N}_i^{\text{Int}} + \bar{N}^{\text{DC}}}{\eta_{\text{RX}} T_i + \eta_{\text{RX}} \bar{N}_i^{\text{Int}} + \bar{N}^{\text{DC}}}, \quad (32)$$

where \bar{N}^{DC} is the mean dark-count number, arising from thermal noise, electrical shot noise, and leakage at the quantum receiver. Optical shot noise can be neglected as it scales with the optical power and is therefore significantly weaker than the coexistence-induced interference and dark-count. Neglecting dark-count photons and assuming unitary receiver efficiency we obtain Eq. (16).

APPENDIX C SHOT-NOISE UNITS CONVERSION

The optical interference in CV-QKD protocols is quantified as the excess noise, normalized to the shot-noise variance. The shot-noise variance, expressed in volts squared, is given by [33, Eq. (107)]

$$\sigma_{\text{SN}}^2 = P_{\text{LO}} B_{\text{el}} R_V^2 h f_i, \quad (33)$$

where P_{LO} is the local-oscillator power, B_{el} is the electronic bandwidth, and R_V is the receiver's conversion factor from optical power to volts, defined as the product of the photodetector responsivity and the transimpedance amplification gain.

Balanced photodetectors measure only photons that are mode-matched with the received local-oscillator photons, scaled by the receiver's conversion ratio. Therefore, in the respective polarization, the coexistence-induced excess noise in volts squared within the electronic bandwidth is given by

$$\xi_{\text{coex},i}^{[V^2]} = \frac{P_{\text{LO}} B_{\text{el}} R_V^2 P_i^{\text{Int}}}{2B_{\text{ch}}}, \quad (34)$$

where we consider the noise PSD as white, Gaussian, and constant within the receiver bandwidth, neglecting the receiver's frequency-dependent response. Normalizing Eq. (34) to shot-noise units yields Eq. (18).

Derivations of the remaining excess noise sources appear in [33].

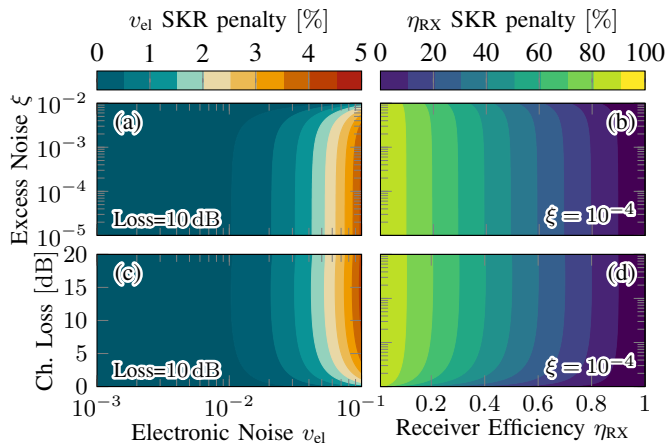


Fig. 14: Secret key rate penalties arising from (a,c) non-zero electronic noise and (b,d) non-ideal receiver efficiency, obtained by sweeping the excess noise in (a,b) and channel loss in (c,d).

APPENDIX D ASYMPTOTIC GMCS SKRS

The derivations provided in this section strongly reference the definitions given in [39, Section III].

The mutual information in GMCS protocols is given by

$$I_{AB} = \frac{\mu}{2} \log_2 \left[1 + \frac{\eta_{RX} T_i V_A}{\eta_{RX} \xi_i + \mu + v_{el}} \right], \quad (35)$$

with $\mu = 1$ for homodyne and $\mu = 2$ for heterodyne detection. where v_{el} is the electronic noise.

The value of χ_{EB} is the Holevo bound between the eavesdropper and the receiver, and is given by

$$\chi_{EB} = h_2(\lambda_+) + h_2(\lambda_-) - h_2(\tilde{\lambda}_+) - h_2(\tilde{\lambda}_-), \quad (36)$$

where λ_{\pm} are the symplectic eigenvalues of the eavesdropper state covariance matrix Σ_E , and $\tilde{\lambda}_{\pm}$ are the same metric for the covariance matrix of the eavesdropper output state conditioned by the receiver's measurement $\Sigma_{E|B}$.

The following subsections derive the asymptotic SKR limits considering ideal reconciliation ($\beta_{EC} = 1$) and noiseless ($v_{el} = 0$) and lossless ($\eta_{RX} = 1$) receiver. Penalties arising from non-ideal receiver devices are shown in Fig. 14 over a practical range of values. They increase nearly linearly with v_{el} and decrease linearly with increasing η_{RX} .

A. Asymptotic limit derivations

The symplectic eigenvalues can be obtained from the absolute ordinary eigenvalues of

$$\lambda_{\pm} = |\text{eig}(j\Omega\Sigma_E)|, \quad \tilde{\lambda}_{\pm} = |\text{eig}(j\Omega\Sigma_{E|B})|, \quad (37)$$

where Ω is a symplectic matrix, given for a 2-mode symbol by [30, Eq. (2)]

$$\Omega = \begin{bmatrix} 0 & 1 & 0 & 0 \\ -1 & 0 & 0 & 0 \\ 0 & 0 & 0 & 1 \\ 0 & 0 & -1 & 0 \end{bmatrix}. \quad (38)$$

The covariance matrix Σ_E is given by the block matrix

$$\Sigma_E = \begin{bmatrix} \omega \mathbf{I} & \psi_1 \mathbf{Z} \\ \psi_1 \mathbf{Z} & \phi_1 \mathbf{I} \end{bmatrix}, \quad (39)$$

where \mathbf{I} is the identity matrix, $\mathbf{Z} = \text{dg}([1, -1])$ with $\text{dg}(\cdot)$ being the diagonal operator, and the remaining parameters are

$$\begin{aligned} \psi_1 &= \sqrt{T_i(\omega^2 - 1)}, \\ \phi_1 &= T_i\omega + (1 - T_i)(V_A + 1). \end{aligned} \quad (40)$$

For a block matrix \mathbf{M} of the following form

$$\mathbf{M} = \begin{bmatrix} \text{dg}([\omega_A, \omega_B]) & \text{dg}([\psi_A, -\psi_B]) \\ \text{dg}([\psi_A, -\psi_B]) & \text{dg}([\phi_A, \phi_B]) \end{bmatrix}, \quad (41)$$

the ordinary eigenvalues λ_M of $j\Omega\mathbf{M}$ are obtained, from determinant properties,⁵ as the solution to

$$\begin{aligned} \lambda_M &= \pm \sqrt{\frac{b' \pm \sqrt{b'^2 - 4c'}}{2}}, \\ b' &= \phi_A \phi_B + \omega_A \omega_B - 2\psi_A \psi_B, \\ c' &= (\phi_A \phi_B - \psi_A \psi_B)(\omega_A \omega_B - \psi_A \psi_B) \\ &\quad - (\psi_A \phi_B - \omega_A \psi_B)(\psi_A \omega_B - \phi_A \psi_B). \end{aligned} \quad (42)$$

For the covariance matrix Σ_E , we have

$$\begin{aligned} \omega_A &= \omega_B = \omega, \\ \psi_A &= \psi_B = \psi_1, \end{aligned} \quad (43)$$

$$\lim_{V_A \rightarrow \infty} \phi_A = \lim_{V_A \rightarrow \infty} \phi_B = \lim_{V_A \rightarrow \infty} \phi_1 \rightarrow (1 - T_i)V_A,$$

and, after some manipulation, the symplectic eigenvalues are given by

$$\lim_{V_A \rightarrow \infty} \lambda_+ \rightarrow \phi, \quad \lim_{V_A \rightarrow \infty} \lambda_- = \omega. \quad (44)$$

1) *Homodyne detection*: For homodyne detection, the parameters for the covariance matrix $\Sigma_{E|B}$ are given by

$$\begin{aligned} \lim_{V_A \rightarrow \infty} \omega_A &= \lim_{V_A \rightarrow \infty} \omega_B = \omega, \\ \lim_{V_A \rightarrow \infty} \psi_A &= \psi, \quad \psi_B = \psi_1, \\ \lim_{V_A \rightarrow \infty} \phi_A &= \phi, \quad \lim_{V_A \rightarrow \infty} \phi_B \rightarrow (1 - T_i)V_A, \end{aligned} \quad (45)$$

with $\psi = \sqrt{(\omega^2 - 1)/T_i}$. The symplectic eigenvalues are then given by

$$\lim_{V_A \rightarrow \infty} \tilde{\lambda}_+ \rightarrow \sqrt{(1 - T)V_A \phi}, \quad \lim_{V_A \rightarrow \infty} \tilde{\lambda}_- = 1. \quad (46)$$

For the limit $V_A \rightarrow \infty$, the elements with I_{AB} , $h_2(\lambda_+)$ and $h_2(\tilde{\lambda}_+)$ in (36) converge⁶ to the logarithm term in Eq. (20).

2) *Heterodyne detection*: For heterodyne detection, the parameters for the covariance matrix $\Sigma_{E|B}$ converge to their unsubscripted values (e.g. $\lim_{V_A \rightarrow \infty} \omega_A = \omega$), and the symplectic eigenvalues are given by

$$\lim_{V_A \rightarrow \infty} \tilde{\lambda}_+ = \frac{\xi + 2 - T}{T}, \quad \lim_{V_A \rightarrow \infty} \tilde{\lambda}_- = 1. \quad (47)$$

For the limit $V_A \rightarrow \infty$, the elements with I_{AB} and $h_2(\lambda_+)$ in (36) converge to the logarithm term in Eq. (24).

⁵Properties:

- $\left| \begin{bmatrix} \mathbf{A} & \mathbf{B} \\ \mathbf{C} & \mathbf{D} \end{bmatrix} \right| = |\mathbf{A}| \cdot |\mathbf{D} - \mathbf{C}\mathbf{A}^{-1}\mathbf{B}|$, if \mathbf{A} is invertible.
- If \mathbf{A}' equals \mathbf{A} when a single row or column is swapped, $|\mathbf{A}'| = -|\mathbf{A}|$.

⁶ $\lim_{x \rightarrow \infty} h_2(x) \rightarrow \log_2(x) + \log_2(e) - 1$

REFERENCES

- [1] H.-K. Lo, M. Curty, and K. Tamaki, "Secure quantum key distribution," *Nature Photonics*, vol. 8, no. 8, pp. 595–604, 2014.
- [2] M. Peev, C. Pacher, R. Alléaume, C. Barreiro, J. Bouda, W. Boxleitner, T. Debuisschert, E. Diamanti, M. Dianati, J. F. Dynes *et al.*, "The SECOQC quantum key distribution network in Vienna," *New journal of physics*, vol. 11, no. 7, p. 075001, 2009.
- [3] M. Sasaki, M. Fujiwara, H. Ishizuka, W. Klaus, K. Wakui, M. Takeoka, S. Miki, T. Yamashita, Z. Wang, A. Tanaka *et al.*, "Field test of quantum key distribution in the Tokyo QKD Network," *Optics express*, vol. 19, no. 11, pp. 10387–10409, 2011.
- [4] S. Wang, W. Chen, Z.-Q. Yin, H.-W. Li, D.-Y. He, Y.-H. Li, Z. Zhou, X.-T. Song, F.-Y. Li, D. Wang *et al.*, "Field and long-term demonstration of a wide area quantum key distribution network," *Optics express*, vol. 22, no. 18, pp. 21739–21756, 2014.
- [5] D. Bacco, I. Vagniluca, B. Da Lio, N. Biagi, A. Della Frera, D. Calonico, C. Toninelli, F. S. Cataliotti, M. Bellini, L. K. Oxenløwe *et al.*, "Field trial of a three-state quantum key distribution scheme in the Florence metropolitan area," *EPJ Quantum Technology*, vol. 6, no. 1, p. 5, 2019.
- [6] P. D. Townsend, "Simultaneous quantum cryptographic key distribution and conventional data transmission over installed fibre using wavelength-division multiplexing," *Electronics Letters*, vol. 33, no. 3, pp. 188–190, 1997.
- [7] N. Peters, P. Toliver, T. Chapuran, R. Runser, S. McNown, C. Peterson, D. Rosenberg, N. Dallmann, R. Hughes, K. McCabe *et al.*, "Dense wavelength multiplexing of 1550 nm QKD with strong classical channels in reconfigurable networking environments," *New Journal of physics*, vol. 11, no. 4, p. 045012, 2009.
- [8] P. Eraerds, N. Walenta, M. Legré, N. Gisin, and H. Zbinden, "Quantum key distribution and 1 Gbps data encryption over a single fibre," *New Journal of Physics*, vol. 12, no. 6, p. 063027, 2010.
- [9] D. Huang, D. Lin, C. Wang, W. Liu, S. Fang, J. Peng, P. Huang, and G. Zeng, "Continuous-variable quantum key distribution with 1 Mbps secure key rate," *Optics express*, vol. 23, no. 13, pp. 17511–17519, 2015.
- [10] T. A. Eriksson, T. Hirano, G. Rademacher, B. J. Puttnam, R. S. Luís, M. Fujiwara, R. Namiki, Y. Awaji, M. Takeoka, N. Wada *et al.*, "Joint Propagation of Continuous Variable Quantum Key Distribution and 18×24.5 Gbaud PM-16QAM Channels," in *2018 European Conference on Optical Communication (ECOC)*. IEEE, 2018, pp. 1–3.
- [11] Y. Mao, B.-X. Wang, C. Zhao, G. Wang, R. Wang, H. Wang, F. Zhou, J. Nie, Q. Chen, Y. Zhao *et al.*, "Integrating quantum key distribution with classical communications in backbone fiber network," *Optics express*, vol. 26, no. 5, pp. 6010–6020, 2018.
- [12] S. Beppu, D. J. Elson, S. Murai, A. Murakami, H. Yamamuro, Y. Wakayama, N. Yoshikane, and T. Tsuritani, "Coexistence Transmission of 33.4-Tb/s O-band Coherent Classical Channels and a C-band QKD Channel over 80 km," in *Optical Fiber Communication Conference*. Optica Publishing Group, 2025, pp. Tu3D–2.
- [13] H. Kawahara, A. Medhipour, and K. Inoue, "Effect of spontaneous Raman scattering on quantum channel wavelength-multiplexed with classical channel," *Optics communications*, vol. 284, no. 2, pp. 691–696, 2011.
- [14] O. Alia, R. S. Tessinari, S. Bahrani, T. D. Bradley, H. Sakr, K. Harrington, J. Hayes, Y. Chen, P. Petropoulos, D. Richardson *et al.*, "DV-QKD coexistence with 1.6 Tbps classical channels over hollow core fibre," *Journal of Lightwave Technology*, vol. 40, no. 16, pp. 5522–5529, 2022.
- [15] S. Du, Y. Tian, and Y. Li, "Impact of four-wave-mixing noise from dense wavelength-division-multiplexing systems on entangled-state continuous-variable quantum key distribution," *Physical Review Applied*, vol. 14, no. 2, p. 024013, 2020.
- [16] L. A. Zischler, Ç. Özkan, T. Vosschenrich, Q. Wu, G. Di Sciullo, D. A. Shaji, C. Lasagni, P. Serena, A. Bononi, A. Ghazisaeidi *et al.*, "Accurate and Effective Model for Coexistence of Classical and Quantum Signals In Optical Fibers," *arXiv preprint arXiv:2510.02807*, 2025.
- [17] L. A. Zischler, A. Ghazisaeidi, C. C. Carrero, T. Vosschenrich, J. Renaudier, A. Mecozzi, and C. Antonelli, "Experimental Characterization and Model Validation of Interference in Classical-QKD Coexistence Transmission," *arXiv preprint arXiv:2602.15910*, 2026.
- [18] J. M. Thomas, F. I. Yeh, J. H. Chen, J. J. Mambretti, S. J. Kohlert, G. S. Kanter, and P. Kumar, "Quantum teleportation coexisting with classical communications in optical fiber," *Optica*, vol. 11, no. 12, pp. 1700–1707, 2024.
- [19] H. H. Brunner, C.-H. F. Fung, M. Peev, R. B. Méndez, L. Ortiz, J. P. Brito, V. Martín, J. M. Rivas-Moscoso, F. Jiménez, A. A. Pastor *et al.*, "Demonstration of a switched CV-QKD network," *EPJ Quantum Technology*, vol. 10, no. 1, p. 38, 2023.
- [20] A. Scherer, B. C. Sanders, and W. Tittel, "Long-distance practical quantum key distribution by entanglement swapping," *Optics express*, vol. 19, no. 4, pp. 3004–3018, 2011.
- [21] P. K. A. Wai and C. Menyak, "Polarization mode dispersion, decorrelation, and diffusion in optical fibers with randomly varying birefringence," *Journal of Lightwave Technology*, vol. 14, no. 2, pp. 148–157, 1996.
- [22] D. Semrau, E. Sillekens, R. I. Killey, and P. Bayvel, "A modulation format correction formula for the Gaussian noise model in the presence of inter-channel stimulated Raman scattering," *Journal of Lightwave Technology*, vol. 37, no. 19, pp. 5122–5131, 2019.
- [23] J.-N. Niu, Y.-M. Sun, C. Cai, and Y.-F. Ji, "Optimized channel allocation scheme for jointly reducing four-wave mixing and Raman scattering in the DWDM-QKD system," *Applied optics*, vol. 57, no. 27, pp. 7987–7996, 2018.
- [24] H. Murata, *Handbook of optical fibers and cables*, 2nd ed. Boca Raton, FL: CRC Press, 1996.
- [25] G. P. Agrawal, *Nonlinear Fiber Optics*, 6th ed. Academic Press, 2019.
- [26] Q. Lin and G. P. Agrawal, "Raman response function for silica fibers," *Optics letters*, vol. 31, no. 21, pp. 3086–3088, 2006.
- [27] R. H. Stolen, J. P. Gordon, W. Tomlinson, and H. A. Haus, "Raman response function of silica-core fibers," *JOSA B*, vol. 6, no. 6, pp. 1159–1166, 1989.
- [28] F. Poletti and P. Horak, "Description of ultrashort pulse propagation in multimode optical fibers," *Journal of the Optical Society of America B*, vol. 25, no. 10, pp. 1645–1654, 2008.
- [29] P. W. Shor and J. Preskill, "Simple proof of security of the BB84 quantum key distribution protocol," *Physical review letters*, vol. 85, no. 2, p. 441, 2000.
- [30] C. Weedbrook, S. Pirandola, R. García-Patrón, N. J. Cerf, T. C. Ralph, J. H. Shapiro, and S. Lloyd, "Gaussian quantum information," *Reviews of Modern Physics*, vol. 84, no. 2, pp. 621–669, 2012.
- [31] C. H. Bennett and G. Brassard, "Quantum cryptography: Public key distribution and coin tossing," in *Proceedings of the IEEE International Conference on Computers, Systems, and Signal Processing, Bangalore, Dec. 1984*, 1984, pp. 175–179.
- [32] F. Grosshans, G. Van Assche, J. Wenger, R. Brouri, N. J. Cerf, and P. Grangier, "Quantum key distribution using gaussian-modulated coherent states," *Nature*, vol. 421, no. 6920, pp. 238–241, 2003.
- [33] F. Laudenbach, C. Pacher, C.-H. F. Fung, A. Poppe, M. Peev, B. Schrenk, M. Hentschel, P. Walther, and H. Hübel, "Continuous-variable quantum key distribution with Gaussian modulation—the theory of practical implementations," *Advanced Quantum Technologies*, vol. 1, no. 1, p. 1800011, 2018.
- [34] M. Milicevic, C. Feng, L. M. Zhang, and P. G. Gulak, "Quasi-cyclic multi-edge LDPC codes for long-distance quantum cryptography," *npj Quantum Information*, vol. 4, no. 1, p. 21, 2018.
- [35] H. Mani, T. Gehring, P. Grabenweger, B. Ömer, C. Pacher, and U. L. Andersen, "Multiedge-type low-density parity-check codes for continuous-variable quantum key distribution," *Physical Review A*, vol. 103, no. 6, p. 062419, 2021.
- [36] S. Walker, "Rapid modeling and estimation of total spectral loss in optical fibers," *Journal of lightwave technology*, vol. 4, no. 8, pp. 1125–1131, 1986.
- [37] A. Alvarado, T. Fehenberger, B. Chen, and F. M. Willems, "Achievable information rates for fiber optics: Applications and computations," *Journal of Lightwave Technology*, vol. 36, no. 2, pp. 424–439, 2018.
- [38] C. Branciard, N. Gisin, B. Kraus, and V. Scarani, "Security of two quantum cryptography protocols using the same four qubit states," *Physical Review A—Atomic, Molecular, and Optical Physics*, vol. 72, no. 3, p. 032301, 2005.
- [39] S. Pirandola and P. Papanastasiou, "Improved composable key rates for CV-QKD," *Physical Review Research*, vol. 6, no. 2, p. 023321, 2024.